Connecting the Local Stellar Halo and Its Dark Matter Density to Dwarf Galaxies via Blue Stragglers

Luca Casagrande[1,2]

[1] Research School of Astronomy and Astrophysics, Mount Stromlo Observatory, Australian National University, ACT 2611, Australia; luca.casagrande@anu.edu.au
[2] ARC Centre of Excellence for All Sky Astrophysics in 3 Dimensions (ASTRO3D), Australia

Abstract

The Gaia H-R diagram shows the presence of apparently young stars at high tangential velocities. Using a simple analytical model, I show that these stars are likely to be blue stragglers. Once normalized to red giant stars, the fraction of nearby halo blue stragglers is of order 20%, and remarkably close to that measured in dwarf galaxies. Motivated by this similarity, I apply to field blue stragglers scaling relations inferred from blue stragglers in dwarf galaxies. Doing this for the Milky Way halo returns an average stellar density of $(3.4 \pm 0.7) \times 10^{-5} M_\odot$ pc^{-3} and a dark matter density of $\simeq 0.006^{+0.005}_{-0.003} \, M_\odot$ pc$^{-3} \simeq 0.22^{+0.20}_{-0.10}$ GeV cm^{-3} within 2 kpc from the Sun. These values compare favorably to other determinations available in the literature but are based on an independent set of assumptions. A few considerations of this methodology are discussed, most notably that the correlation between the dark matter halo core density and stellar mass seems to hold from dwarf galaxies to the nearby Milky Way halo.

Unified Astronomy Thesaurus concepts: Baryon density (139); Dark matter density (354); Blue straggler stars (168); Galaxy stellar halos (598); Dwarf galaxies (416)

Supporting material: animation

1. Introduction

Recent results have shown that the close binary fraction ($P \lesssim 10^4$ days and $a \lesssim 10$ au) of solar-type stars is anticorrelated with metallicity (El-Badry & Rix 2019; Moe et al. 2019), implying that most solar-type stars with [Fe/H] < −1 will interact with a close binary. While the implications of this results are manyfold, here I focus on the rate of blue straggler stars (BSSs). First observed by Sandage (1953) in the globular cluster M3 as an apparent extension of the classical main sequence, BSSs are now believed to be the product of mass transfer and/or merger in close binaries or multiple-star systems (e.g., Knigge et al. 2009; Santana et al. 2013). The metallicity anticorrelation of close binaries implies that the fraction of BSSs is expected to increase at decreasing metallicity (Wyse et al. 2020). This means that the BSSs population should become more prominent when moving to increasingly metal-poor and old populations (so that BSSs can be readily identified populating the left-hand side of the turnoff), such as moving from the thin to the thick disk and halo. Here I use data from Gaia DR2 (Gaia Collaboration et al. 2018b) and simple analytical considerations to show that this identification is indeed possible. The fraction of BSSs found at high tangential velocities is in excellent agreement with that measured in dwarf spheroidal and ultrafaint dwarf galaxies. For these stellar systems, the fraction of BSSs is proportional to their total stellar mass (Santana et al. 2013), which then correlates to their dark matter halo core density. Here I show that by applying these relations to the BSSs identified in the Galactic stellar halo, it is possible to obtain measurements of the local stellar and dark matter density that are in agreement with those derived by other means. This result supports the assumption of applying to the halo of a spiral galaxy like the Milky Way scaling relations for BSSs in dwarf galaxies. Thus, field BSSs might be able to provide a new diagnostic to study the stellar and dark matter density in the halo. A number of methodologies have been developed over the years to measure

these two densities, which are central, e.g., to guide direct dark matter detection experiments, to understand the formation of the Milky Way and to place it in the cosmological context with other, similar-mass galaxies (e.g., Read 2014; Deason et al. 2019; de Salas 2020). However, these measurements are far from definitive. For the stellar density in the halo, a wide range of local normalizations have been reported in the literature. Local dynamical dark matter density measurements are strongly affected by the imperfect knowledge of the baryonic contribution, and in spite of the data from Gaia, different analyses still return dissimilar results (e.g., Sivertsson et al. 2018; de Salas 2020). The use of BSSs to derive stellar and dark matter densities is explored here by developing a methodology that is based on assumptions largely different from those used by other methods.

2. Blue Straggler Selection

From Gaia DR2 I retrieve all stars satisfying conditions 1, 2, and 3 of Arenou et al. (2018), and with parallax errors below 10%, totaling 67.7 million objects. These requirements are also used in Gaia Collaboration et al. (2018a) to study the fine structure of the Hertzsprung–Russell diagram, removing most of the artifacts while still allowing us to see the imprint of genuine binaries. Avoiding selection against binaries might be relevant given that Preston & Sneden (2000) concluded that a significant fraction of BSSs are binaries. For this same reason I do not impose a threshold on the Renormalized Unit Weight Error (RUWE; technical note GAIA-C3-TN-LU-LL-124-01) and note that the present sample has a median RUWE of 1.0, with 97% of the stars having RUWE < 1.4.

BSSs are identified in a fashion similar to Santana et al. (2013) and normalized to the number of red giant branch (RGB) stars identified in a similar range of absolute magnitudes. The advantage of using the number count of stars selected in a similar range of intrinsic luminosities is that their ratio is largely insensitive to
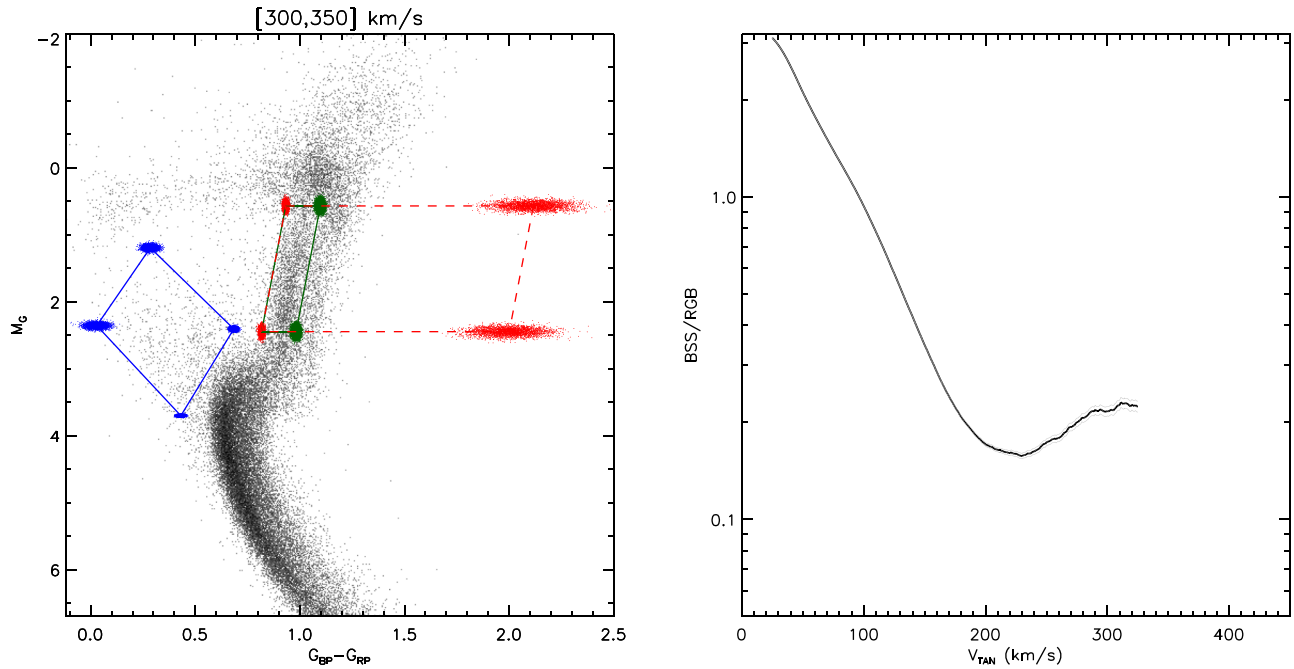
Figure 1. Left panel: color–magnitude diagram for the Gaia sample having tangential velocities (V_{TAN}) in the range indicated on the top of the panel. Colors and magnitudes have been corrected for reddening as described in the text. The blue and red boxes are used to identify BSSs and RGB stars, respectively. The green box is used to identify bRGB stars (i.e., RGB stars on the Gaia blue sequence; see description in Section 4). Scattered blue, red, and green points are the range of values explored for the 10,000 Monte Carlo realizations described in the paper. Right panel: black line shows the ratio of stars falling into the BSS and RGB boxes when selecting them in a moving V_{TAN} boxcar of width 50 km s^{-1}. Solid gray lines are 1σ Poisson error bars. The point with the highest V_{TAN} in this figure is obtained doing the ratio of the BSSs and RGB stars shown in the left panel. An animation of these panels, with a V_{TAN} boxcar running from 0 to 500 km s^{-1}, is available. The duration of the video is 50 s.

(An animation of this figure is available.)

selection effects stemming from the Malmquist bias (Malmquist 1922).

BSSs and RGB stars are defined as stars falling within the blue and red boxes shown in the color–magnitude diagram of Figure 1. These boxes are obtained following Evans et al. (2018) to convert gr magnitudes from Santana et al. (2013) into the Gaia photometric system, plus small zero-point shifts to optimize these boxes with the actual position occupied by BSSs and RGB stars in the Gaia H-R diagram. For the RGB box, the boundary at cool temperatures is extended to colors redder than in Santana et al. (2013), to account for a range of metallicities and ages in the Galactic disk that is much larger than that encountered in dwarf galaxies or globular clusters. This extension is, however, irrelevant when dealing with stars at high tangential velocities, which occupy the leftmost position on the RGB box (see also animation associated with Figure 1). Gaia colors and magnitudes of all stars have been corrected for reddening using a rescaled version of the Schlegel et al. (1998) map as described in Kunder et al. (2017), with reddening coefficients from Casagrande & VandenBerg (2018).

The video associated with Figure 1 shows how the ratio of the number of stars falling into the BSS and RGB boxes varies when selecting stars with different tangential velocities. As V_{TAN} increases, the dominant stellar population changes from the thin to the thick disk, until the ratio remains constant at a value of 0.2–0.3 for tangential velocities that are typical of halo stars.

The box used to identify BSSs suffers from contamination from main-sequence stars populating this region of the H-R diagram. This effect is very strong in a young stellar population

like the thin disk (say, $V_{TAN} < 40$ km s^{-1}; see, e.g., Gaia Collaboration et al. 2018a) and decreases when moving toward older populations like the thick disk and halo. Figure 1 is obtained using all stars without any restriction on their Galactic latitude b or height above the Galactic plane Z. Another source of uncertainty is due to the arbitrary definition of the BSS and RGB boxes, as well as to the reddening corrections applied. To account for all these uncertainties, I run 10,000 Monte Carlo realizations where each time I randomly changed the boundaries of the BSS and RGB boxes by up to several hundreds of mag, reddening by 20%, let the width of the boxcar vary anywhere between 10 and 60 km s^{-1}, and considered only stars with heights above the Galactic plane varying in the range $0 < Z < 400$ pc. The results are shown in the left panel of Figure 2. At low V_{TAN} the ratio of stars falling into the BSS and RGB boxes varies quite substantially, and this is largely driven by the adopted cuts in Z. The higher stars are above the Galactic plane, the lower is the contamination from young thin-disk stars that otherwise would fall into the BSS box. Therefore, the ratio of stars into the BSS and RGB boxes decreases. I verified that very similar results are obtained if doing a cut in the projected height above the plane, i.e., Galactic latitude b, instead of Z.

Remarkably, the trend reverses for tangential velocities around 200 km s^{-1} and the ratio becomes nearly constant above $\sim$300 km s^{-1}, with very low scatter independently of the set of parameters of each Monte Carlo realization.

3. Analytical Model

The number of main-sequence stars that contaminate the BSS box relative to the RGB one can be modeled generating a
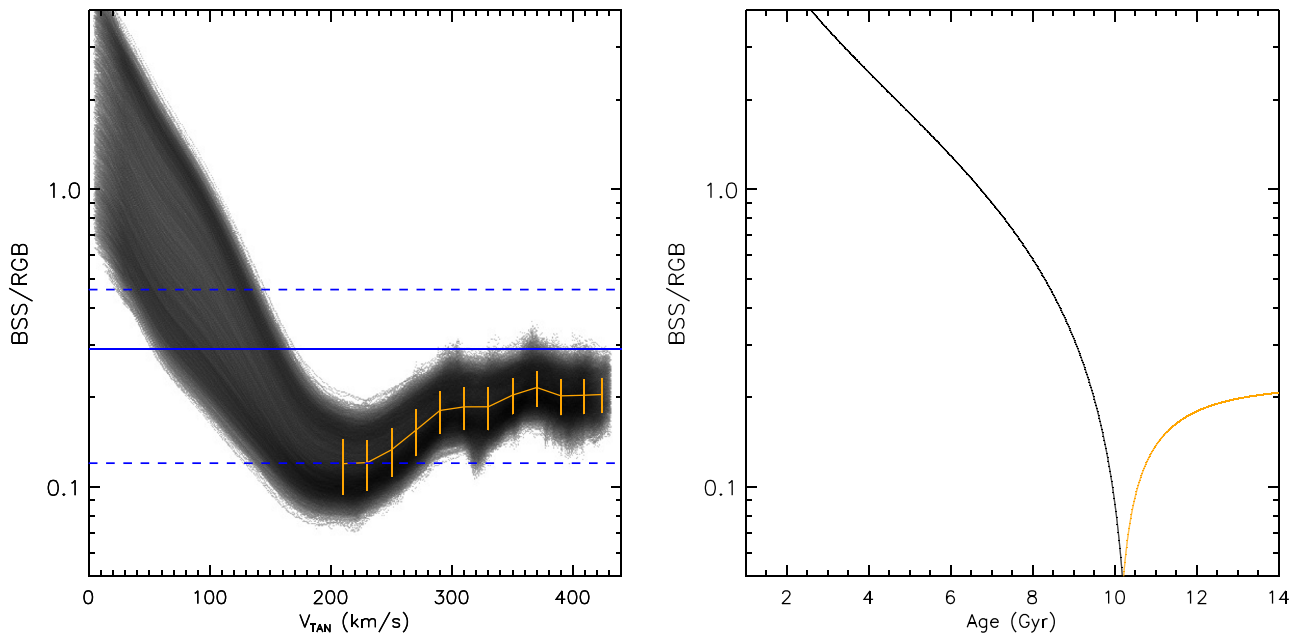
Figure 2. Left panel: BSS-to-RGB ratio as a function of V_{TAN} for 10,000 Monte Carlo realizations varying parameters as described in the text (gray lines). The orange line is the mean and standard deviation of all realizations above 200 km s^{-1}. The solid blue line is the BSS-to-RGB ratio measured by Santana et al. (2013) for dwarf galaxies, with 1σ uncertainties indicated by the dashed lines. Right panel: analytic models of Equations (4) (black) and (5) (orange).

synthetic stellar population, but this is beyond the scope of this analysis. Instead, simple analytical considerations suffice to understand the trend.

The number of main-sequence stars that fall into the BSS box at any given time is given by

$$N_{BSS} = \int_{M_1}^{M_2} \phi(m) dm, \quad (1)$$

where $\phi(m)$ is the initial mass function (IMF) and M_1 and M_2 are minimum and maximum stellar mass in the BSS box. For stars above roughly a solar mass, the IMF slope of Salpeter (1955) can be safely used, i.e., $\phi(m) \propto m^{-2.35}$. Similarly, the number of stars that are on the RGB phase at a given time is given by all stars massive enough to have evolved off the main sequence, i.e., with masses higher than the time-dependent turnoff mass $M(t)$. The latter can be readily derived from the relationship between main-sequence lifetime and stellar mass (e.g., Kippenhahn et al. 2012):

$$\frac{M(t)}{M_\odot} \sim \left(\frac{t}{t_\odot}\right)^{-1/3}. \quad (2)$$

This implies that at any given time the following ratio R' holds between newly formed stars that fall in the BSS and RGB selection boxes:

$$R' = \frac{\int_{M_1}^{M_2} \phi(m) dm}{\int_{M(t)}^{\infty} \phi(m) dm} = \frac{M_1^{-1.35} - M_2^{-1.35}}{(t/t_\odot)^{0.45}}. \quad (3)$$

For practical purposes, the power law of the IMF implies that the upper limit of integration at the denominator goes quickly toward a negligible contribution, be it a few tens of solar masses or infinity. If one wishes instead to derive the ratio R between all stars formed until a given time that fall onto the BSS and RGB boxes, it suffices to integrate over t and to

correct for the stars that have evolved off the selection boxes. For the BSS box, this implies removing all stars that have evolved off the main sequence, i.e., with masses in the range $M(t)$ to M_2. For the RGB box, one should correct for all stars that have left the giant branch. At a given age, the RGB spans a mass range that is of order of a few percent of the turnoff mass, $p \sim 1.1$–1.03:

$$R = \frac{\int_0^t \left[\int_{M_1}^{M_2} \phi(m) dm - \int_{M(t)}^{M_2} \phi(m) dm\right] dt}{\int_0^t \int_{M(t)}^{p\,M(t)} \phi(m) dm\, dt}$$

$$= \frac{1.45\, M_1^{-1.35} - (t/t_\odot)^{0.45}}{(1 - p^{-1.35})(t/t_\odot)^{0.45}}. \quad (4)$$

Here the integration over time corresponds to assuming a constant star formation history, which suffices to describe most of the evolution of the Galactic disk, at least over the past ~8 Gyr (e.g., Snaith et al. 2015) The dependence of Equation (4) with time is shown in the left panel of Figure 2, where I have used isochrones for an informed guess on M_1. I have adopted the MIST isochrones (Choi et al. 2016) with $-2.0 \leqslant [Fe/H] \leqslant 0.5$ (roughly the range of metallicities covered by stars with $V_{TAN} < 200$ km s^{-1}; e.g., Sahlholdt et al. 2019) and with ages spanning over the entire grid of MIST isochrones. I have then identified all isochrone masses that fall in the BSS box of Figure 1, obtaining the values $M_1 = 1.0$ and $M_2 = 1.8$ for the 10th and 90th percentiles, respectively.

Stars with $V_{TAN} > 200$ km s^{-1} typically have ages older than ~10 Gyr and belong to the kinematically hot tail of the thick disk and to the stellar halo (e.g., Di Matteo et al. 2019; Helmi et al. 2018; Sahlholdt et al. 2019). The simple model of Equation (4) is sufficient to inform that at these old ages there

will not be residual main-sequence stars falling into the BSS box. This reinforces the interpretation that the majority of stars identified in the BSS box with $V_{TAN} \gtrsim 200 \, km \, s^{-1}$ are genuine BSSs.

The constant ratio of BSSs at high V_{TAN} can also be qualitatively understood. I assume $0.8 M_\odot$ as the typical stellar mass for halo (sub)giant stars (e.g., Epstein et al. 2014; VandenBerg et al. 2014), and I further assume that if a star occupies the BSS box, it must roughly be $>1 M_\odot$ (as supported by the isochrones check done above). The number of BSSs with final mass $>1 M_\odot$ is given by a fraction of all possible combinations of mass for stars between $M_a = 0.2$ and $M_b = 0.8 M_\odot$, and which are in a binary system. Adopting the Kroupa (2001) IMF (whose broken power law is more appropriate than the Salpeter one for masses below $M_K = 0.5 M_\odot$) leads to

$$
\begin{aligned}
R &= f_c \, f_m \frac{\int_{t_2}^{t} \int_{M_a}^{M_b} \phi(m) \, dm \, dt}{\int_{t_1}^{t} \int_{M(t)}^{p \, M(t)} \phi(m) \, dm \, dt} \\
&= 1.43 f_c \, f_m \, t_\odot^{0.43} \frac{(t - t_2)}{(t^{1.43} - t_1^{1.43})} \\
&\quad \times \frac{\frac{4}{15}(M_a^{-0.3} - M_K^{-0.3}) + \frac{2}{65}(M_K^{-1.3} - M_b^{-1.3})}{\frac{2}{65}(1 - p^{-1.3})}.
\end{aligned}
\tag{5}
$$

Here the number of RGB stars is given by the number of objects in the appropriate mass range that formed at least $t_1 = 9$ Gyr ago, where this age corresponds to a turnoff mass of $\sim 0.8 M_\odot$ (Equation (2)). Moving to the number of BSSs, I do not make any assumption when their mergers occur (which in fact could happen at times more recent than t_1), nor their formation channels (e.g., binary interaction when both components are still on the main sequence, but also from interaction with an evolved primary with a mass somewhat higher than M_b). There is a degree of stochasticity in the time at which each binary merger will occur, besides the effect of stellar lifetime in the range M_a–M_b, and of stragglers in the range M_1–M_2 (which will then evolve toward the giant phase). Modeling these effects goes beyond the analytical formulation presented here. The net effect of decreasing the number of BSSs at any given time can be expressed as a delay, where the number of BSSs will start to increase linearly from $t_2 > t_1$. Choosing, e.g., $t_2 = 10$ Gyr produces a smooth slope similar to what is seen at V_{TAN} between 200 and 300 km s^{-1}. For $t_2 = t_1$ the rise is much steeper, although irrelevant for the qualitative sake of this discussion.

Only a certain fraction of all possible mass combinations in the range 0.2–$0.8 M_\odot$ will result in a sum $>1 M_\odot$, and this is accounted for by f_c. This correction factor is determined numerically, by generating a distribution of masses according to the adopted IMF, and for a given fraction of binaries f_b computing how many will have a total mass $>1 M_\odot$. This returns $f_c \sim 0.18 f_b$, where f_b can be taken from observations. The only free parameter is thus f_m, which is the fraction of binaries undergoing mass transfer/merger. This can be determined by requiring the plateau at old ages of Equation (5) to match that observed in the halo (Figure 2). Decent agreement is obtained if $f_c \, f_m = 0.18 f_b \, f_m = 0.018$. Adopting $f_b = 0.5$ for the fraction of metal-poor close binaries (Moe et al. 2019) implies $f_m = 0.2$, i.e., 20% of close binaries (or equivalently 10% of stars) will undergo some sort of mass transfer and/or merger. Note that different values of

binary fraction will vary the percentage of binaries undergoing mass transfer (e.g., $f_b = 0.4$ implies $f_m = 0.25$), but the total fraction of stars ($f_b \, f_m$) remains unchanged at 10%.

The purpose of this analytical formulation is simply to show that with a few basic assumptions on the IMF and stellar lifetimes, it is possible to qualitatively describe the trend seen in the BSS-to-RGB ratio of Figures 1 and 2. At low V_{TAN} (i.e., young and intermediate-age stellar populations) the trend reflects the number of main-sequence versus RGB stars. The flattening seen at high V_{TAN} (old populations) can instead be described assuming that stars in the BSS box are created by stellar mergers with a set of reasonable parameters.

4. Building a Volume-complete Sample of Halo Blue Stragglers

Membership to the stellar halo based only on V_{TAN} is rather approximate. Gaia Collaboration et al. (2018a) have revealed that stars with $V_{TAN} > 200 \, km \, s^{-1}$ fall along two well-defined sequences separated by roughly 0.1 mag in color, dubbed the red and blue sequence. At $V_{TAN} = 200 \, km \, s^{-1}$ there is still a clear contribution of thick-disk stars falling onto the red sequence, and the stellar halo becomes clearly dominant only above $V_{TAN} = 250$–$300 \, km \, s^{-1}$ (see Figure 5 in Sahlholdt et al. 2019). The blue sequence has been speculated to be formed by stars accreted by one (or more) massive dwarf galaxy, whereas the red sequence likely comprises the tail of the thick disk, kinematically heated by the accretion event (e.g., Di Matteo et al. 2019; Haywood et al. 2018; Helmi et al. 2018; Koppelman et al. 2019; Myeong et al. 2019; Sahlholdt et al. 2019).

The BSS-to-RGB ratio in the left panel of Figure 2 bottoms off and reverses between 200 and 300 km s^{-1}, after which it stabilizes to a mean (and median) value of 0.20 with a standard deviation of 0.03. This value is remarkably robust and well within the range measured by Santana et al. (2013) in dwarf galaxies with no recent star formation (0.29 with a standard deviation of 0.17), with selection boxes similar to those adopted here.[1] Whether or not the local halo is formed by one or more disrupted dwarf galaxies, it might not come as a surprise that the density of BSSs in low-metallicity, low-density environments, such as the Galactic halo and dwarf galaxies, is similar (see e.g., Momany et al. 2007).

Santana et al. (2013) report a correlation between the number of BSSs in a dwarf galaxy and the total stellar mass of the system (their Equation (5)). Motivated by the constant BSS-to-RGB ratio found at high tangential velocities and its similarity to that measured in dwarf galaxies, I use the aforementioned correlation to test whether it returns a sensible estimate for the stellar mass in the local halo. To successfully do so, it is crucial to correctly assign BSSs to the halo. This is not trivial to do purely based on V_{TAN} because of contamination from the thick disk above 200 km s^{-1} and the fact that the halo extends below this velocity. The blue sequence of the Gaia H-R diagram offers a way out.

I define an RGB to be a member of the Gaia blue sequence (bRGB) if it falls on the green box of Figure 1. This box is contained within the RGB box, and its boundaries on the right-hand side have been defined selecting the midpoint where the

---

[1] As in Santana et al. (2013), I use the BSS-to-RGB ratio (R) at face value. The actual value will be slightly higher, $R/(1 - R)$ under the assumption that a fraction R of RGB stars are in fact evolved BSSs. At the same time, the measured R is an upper limit, since the adopted box does not extend to the tip of the RGB.
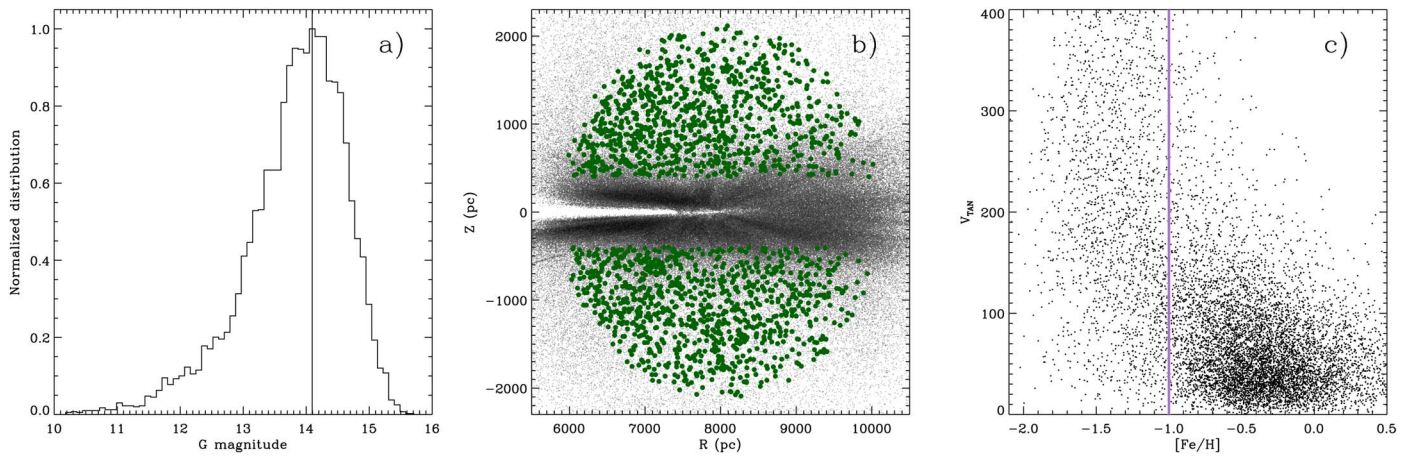
Figure 3. Left panel: distribution of Gaia G magnitudes for stars into the bRGB box, with $|Z| > 400$ pc and $V_{\mathrm{TAN}} > 250$ km s^{-1}. The vertical line is the mode of the distribution. Middle panel: the gray density plot is the distribution of all stars into the bRGB box as a function of height from the Galactic plane Z and Galactocentric distance R (assuming that the Sun is 8 kpc from the Galactic center; Gravity Collaboration et al. 2019). Green circles are bRGB stars with $|Z| > 400$ pc and $V_{\mathrm{TAN}} > 250$ km s^{-1} and closer than $\sim$2 kpc. Right panel: [Fe/H] vs. V_{TAN} for bRGB stars in the SkyMapper sample with $|Z| > 400$ pc and closer than $\sim$2 kpc. Stars with metallicities below -1 (vertical line) are classified as halo.

Gaia red and blue sequences are most separated in the H-R diagram of high-V_{TAN} stars (in a fashion similar to Sahlholdt et al. (2019). This is best appreciated in the animation of Figure 1). This region encompasses mostly old, metal-poor red giants from the halo, although younger and more metal-rich red giant stars from the Galactic disk can contaminate it, especially at low V_{TAN}. I use metallicities from the SkyMapper photometric survey (Casagrande et al. 2019) to identify halo stars purely from their chemistry, and I estimate the fraction of missing halo stars when cutting at a given V_{TAN} and height Z. With this correction, I then derive a volume-complete number of halo bRGB stars and use the constant BSS-to-RGB ratio of Figure 2 to estimate the number of halo BSSs and total stellar mass within the same volume through Equation (5) of Santana et al. (2013). It can be seen from the animation of Figure 1 that at the highest V_{TAN} (where the halo sample is the cleanest, with all RGB stars virtually on the blue sequence) the BSS-to-RGB ratio remains constant at 0.2. This indicates that contamination from thick-disk stars affects equally BSSs and RGB stars (not unexpectedly, since they have similar intrinsic luminosities and hence probe similar distances), and their ratio is thus a robust quantity.

Below, all these steps are explained in detail with a case study, using a set of fixed parameters. This procedure is then generalized using 100,000 Monte Carlo realizations, where the parameters adopted in the case study are changed within a reasonable range.

Gaia DR2 parallaxes have a typical precision of order 0.04 mas for stars brighter than $G \sim 15$ (which is appropriate for the bulk of this sample). This, together with the requirement of 10% precision in parallaxes (Section 2), limits completeness to parallaxes $\gtrsim$0.4 mas (or distances closer than about 2.5 kpc). This estimate, however, does not account for the fact that stars with different intrinsic luminosities will be complete to different distances. The distribution of G magnitudes for bRGB shows the typical power law of a uniform, volume-complete sample up to $G \simeq 14.1$ (Figure 3(a)). The green box of Figure 1 requires a complete sampling of bRGB stars to be sensitive to $M_G \sim 2.5$, thus implying that $D = 10^{\frac{14.1-2.5}{5}-2} \sim 2$ kpc is the farthest distance at which the sample is complete. At bright magnitudes Gaia DR2 is complete down to $G \sim 7$ (see

discussion in Gaia Collaboration et al. 2018b; Bennett & Bovy 2019), which, together with the bright limit of $M_G \sim 0.6$ for the bRGB box, translates to a distance completeness of $\sim$190 pc. This limit is of no concern since I only select stars with $|Z| > 400$ pc, to avoid regions heavily affected by reddening and crowding, as well as strong contamination from the disk (this cut in Z eliminates all bRGB stars within $\sim$10° from the Galactic plane). There are 1824 bRGB stars satisfying these criteria.

SkyMapper provides [Fe/H] for some 9 million stars in the southern sky, with no selection other than having good photometry, in a color range that well encompasses the RGB box, and Galactic latitudes $|b| > 5°$ (Casagrande et al. 2019). All stars from the SkyMapper sample are in Gaia DR2: I apply the quality flags and reddening corrections described in Section 2 and identify SkyMapper members of the Gaia blue sequence with $|Z| > 400$ pc using the same green selection box of Figure 1. Also for this sample restricting to distances closer than 2 kpc is appropriate (the distribution of G magnitudes for the SkyMapper sample peaks at a value similar to that of the Gaia sample). Figure 3(c) shows that within the bRGB box there is a considerable fraction of metal-rich giants, as well as metal-poor stars with $V_{\mathrm{TAN}} < 250$ km s^{-1}. I classify a star as halo if its [Fe/H] < -1, and I define the following correction for the fraction of missing halo stars:

$$ f_{\mathrm{ma}} = 1 - \frac{n_{V_{\mathrm{TAN}}>250}^{|Z|>400}}{n_{[\mathrm{Fe/H}]<-1}^{|Z|>400}}, \tag{6} $$

where the numerator and denominator are the number of bRGB stars 400 pc above the Galactic plane with tangential velocities above 250 km s^{-1} and metallicities below -1, respectively. I find that $f_{\mathrm{ma}} \sim 0.6$, i.e., within 2 kpc about 60% of halo stars are lost when cutting at $V_{\mathrm{TAN}} > 250$ km s^{-1} and $|Z| > 400$ pc. Thus, the complete number of halo bRGB stars is of order 4500. The choice of using [Fe/H] < -1 to chemically assign stars to the halo is arbitrary, and the transition from the thick disk and halo is not clear-cut (e.g., Reddy & Lambert 2008; Ruchti et al. 2010; Sahlholdt et al. 2019). Nevertheless, from Figure 3(c) it is clear that at the highest V_{TAN} (where the
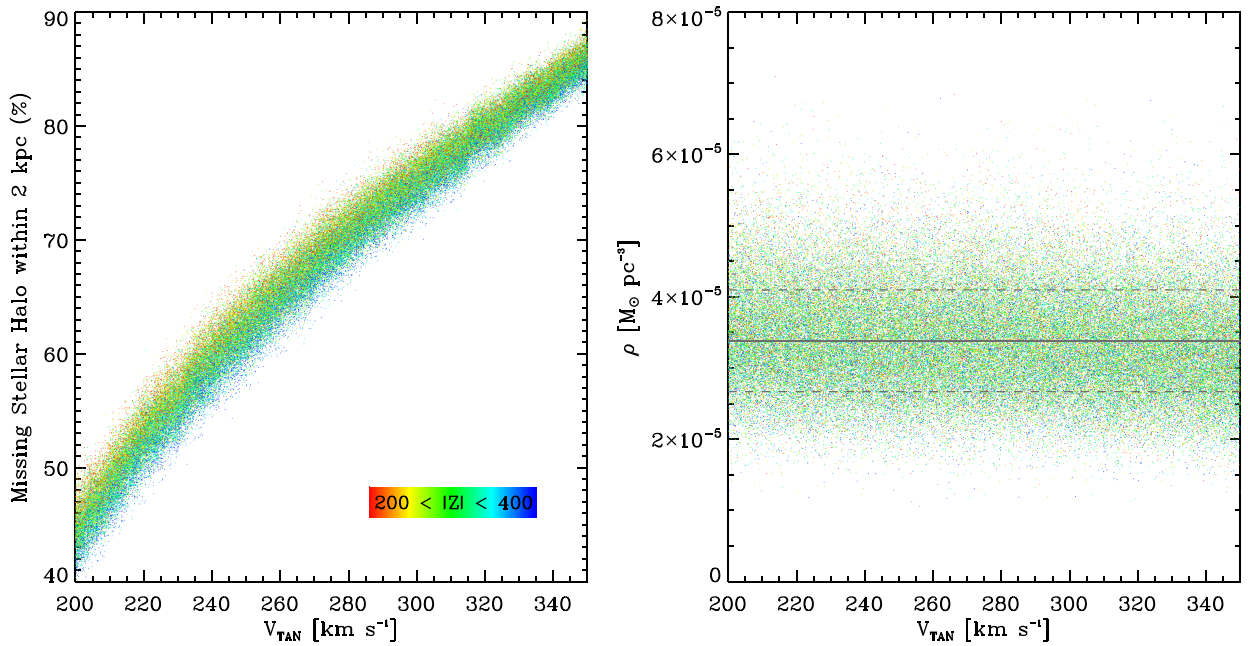
Figure 4. Left panel: fraction of missing halo bRGB stars as a function of $V_{\rm TAN}$, for different cuts in height Z above the Galactic plane (shown in color). Each point is one of the 100,000 Monte Carlo realizations of the procedure described in the text. Right panel: stellar halo density from each realization. Gray lines mark the mean (solid line) and 1σ levels (dotted lines).

fraction of genuine halo stars is the highest) the bulk of stars has $[{\rm Fe/H}] < -1$. Also, the adopted choice is consistent with the literature, where the broad metallicity distribution of the halo is found to become prominent below -1 (e.g., Ryan & Norris 1991; An et al. 2013), whereas at high $V_{\rm TAN}$ the thick disk peaks at -0.7 (Sahlholdt et al. 2019).

It must be noted that the completeness of the samples is partly decreased by the quality cuts described in Section 2. To assess their effect, I query the Gaia archive requiring only parallaxes better than 10%. This results in a sample of about 72.5 million objects, i.e., about 7% larger than the one used in Section 2. This is consistent with the order 10% effect found by Bennett & Bovy (2019) when introducing quality cuts on a sample with parallaxes better than 20%. If I only consider stars in a color range broadly consistent with the location of the BSS $(0 < G_{\rm BP} - G_{\rm RP} < 0.8)$ and RGB $(0.7 < G_{\rm BP} - G_{\rm RP} < 1.3)$ boxes, the mean and median difference of the two samples as a function of Galactic latitude is 6%, with a scatter of 4%. This check is to ensure the absence of significant trends with latitude, due to the fact that the quality flag `phot_bp_r-p_excess_factor` is sensitive to increasing stellar crowding toward the plane of the Galaxy (Evans et al. 2018).

I thus increase by 6% the number of halo bRGB stars and convert those into the expected number of halo BSSs using a fraction of 0.20 from Figure 2. Using Equation (5) from Santana et al. (2013), I estimate a total halo stellar mass of $0.9 \times 10^6 M_\odot$ within $\sim$2 kpc from the Sun. Accounting for the volume of a missing spherical segment of height $\pm Z$,

$$V = \frac{\pi Z}{3}(6D^2 - 2Z^2), \qquad (7)$$

where $D = 2$ kpc and $Z = 0.4$ kpc, returns a local stellar halo density $\rho = 3.4 \times 10^{-5} M_\odot$ pc^{-3}.

The procedure outlined above is repeated 100,000 times, varying each time with Gaussian random errors the boundaries of the bRGB box (Figure 1), reddening by 20%, parallaxes

within their quoted errors, completeness correction by 6% $\pm$ 4%, and imposing different cuts in $200 < |Z({\rm pc})| < 400$ and $200 < V_{\rm TAN}({\rm km\,s}^{-1}) < 350$. A correction for the fraction of missing halo bRGB stars is determined each time, by similarly perturbing for the SkyMapper sample reddening, parallaxes, and metallicities by 0.2 dex. The mode of the distribution of G magnitudes is determined for the Gaia and the SkyMapper sample, and the brightest of the two is used to find the farthest distance at which both samples are complete given the faintest M_G of the bRGB box used. The correction for the fraction of missing halo bRGB stars is applied to derive the actual number of halo bRGB stars, which is then converted into a number of BSSs using a ratio of 0.20 ± 0.03.

From the procedure described above, I obtain the following value for the average stellar halo density within 2 kpc from the Sun (Figure 4):

$$\rho = (3.4 \pm 0.7) \times 10^{-5} M_\odot \ {\rm pc}^{-3}. \qquad (8)$$

While the correction for the fraction of missing halo bRGB stars is a strong function of $V_{\rm TAN}$, ρ is remarkably flat, as one would expect after applying a proper completeness correction. A wide range of density normalizations have been found in the literature $((3-15) \times 10^{-5} M_\odot \ {\rm pc}^{-3}$; Morrison 1993; Fuchs & Jahreiß, 1998; Gould et al. 1998; de Jong et al. 2010). The value derived here compares more favorably to low normalizations, although the very different values obtained by different authors over the years highlight how difficult it is to derive a definitive measurement.

It must be noted that the relation of Santana et al. (2013) is not exactly linear between the number of BSSs and stellar mass. In other words, the stellar mass of a dwarf galaxy with n BSSs is different from the mass of m dwarf galaxies, each containing i BSSs $\sum i = n$. In the extreme (and unrealistic) case that each BSS comes from a different dwarf galaxy, the difference with respect to assuming all from the same dwarf amounts to $1 - n^{-0.11}$, or about 50% for $n \sim 10^3$. Recent
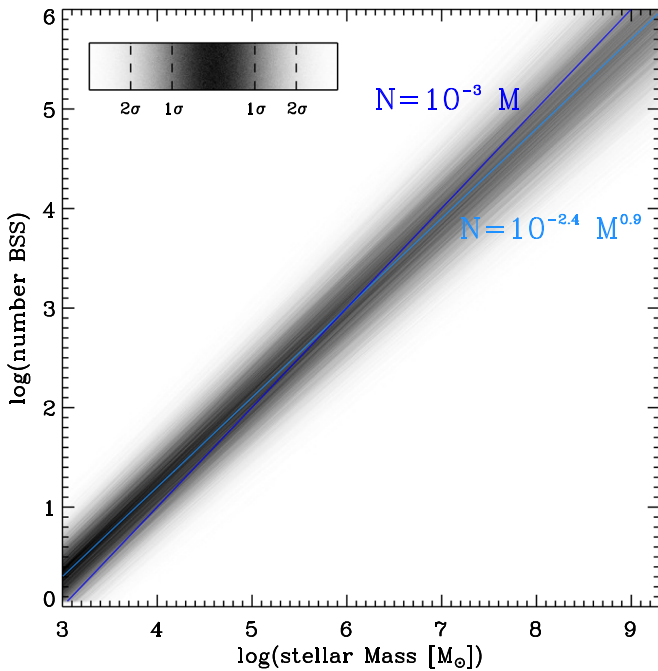
Figure 5. Relation between the number of BSSs and the stellar mass of a dwarf galaxy from Santana et al. (2013) (light blue). The region allowed by the uncertainties of the relation is shown in gray (with 1σ and 2σ levels indicated in the upper bar). A linear relation that still fits within the errors is shown by the dark-blue line.

evidence suggests that the local Galactic halo is the result of two or few massive mergers (e.g., Myeong et al. 2019), in which case the difference reduces to the order of some percent. However, we do not know the total number of BSSs, of which only a fraction is observed within 2 kpc. Fortunately, Figure 5 shows that the relation of Santana et al. (2013) can be well approximated with a linear function within its uncertainties. Adopting the linear form of Figure 5, the inferred stellar halo density increases at the percent level only. It should be pointed out that the relation of Santana et al. (2013) is calibrated between $\sim 10^3$ and $\sim 10^6 M_\odot$, and here it has been applied within this range. The comparison of the linear function in Figure 5 extends up to $10^9 M_\odot$ (the total stellar mass of the halo; e.g., Deason et al. 2019). While it must be explored whether the adopted linear relation holds to this regime, the point here is that while different linear functions will change somewhat the stellar mass derived, the effect is within the quoted uncertainties.

5. Scaling Relations

The good agreement of the local baryon density with estimates from the literature from the previous section warrants further investigation of whether scaling relations derived from BSSs in dwarf galaxies can be applied to the Milky Way halo. Figure 6 shows the volume density of BSSs as a function of stellar density for both dwarf galaxies (solid blue line) and globular clusters (solid red line) from Santana et al. (2013). Stellar densities have been calculated within a half-light radius, using $0.5\, L_V/L_{\odot,V}$ from Muñoz et al. (2018), and assuming a stellar mass-to-light ratio of $M_\star/L_V = 1.5 M_\odot/L_{\odot,V}$. This value is appropriate for both dwarf galaxies and globular clusters in this sample (e.g., Woo et al. 2008; Baumgardt & Hilker 2018). I have used half-light radii from Sérsic profiles $R_{h,s}$ since in

Muñoz et al. (2018) those are available for both dwarf galaxies and globular clusters, and note here that differences are negligible for systems having half-light radii from exponential or Plummer profiles. I multiply by two-thirds the number of BSSs in Santana et al. (2013) since those are counted up to two half-light radii.[2]

The density of BSSs steeply correlates with stellar density in both dwarf galaxies and globular clusters. For dwarf galaxies, the intercept of the relation with the density of halo BSSs determined in the previous section returns a stellar density of $(3.1 \pm 0.5) \times 10^{-5} M_\odot\, \mathrm{pc}^{-3}$. The good agreement with the value previously determined is not unexpected, both ultimately depending on the same set of data. However, it must be noted that the choice of comparing the density of halo BSSs to that within a half-light radius of dwarf galaxies is arbitrary. If stellar densities were to be computed within two half-light radii, the stellar density inferred for the halo would change to $(2.6 \pm 0.6) \times 10^{-5} M_\odot\, \mathrm{pc}^{-3}$. Not unexpectedly, the largest source of systematic uncertainty is the adopted stellar mass-to-light ratio, where a change of $\pm 0.5 M_\odot/L_{\odot,V}$ affects stellar densities by $\pm 1.0 \times 10^{-5} M_\odot\, \mathrm{pc}^{-3}$.

More interestingly, the density of BSSs is found to correlate with the dark matter density of dwarf galaxies, here computed again within a half-light radius. This can be understood from the dark matter scaling laws in late-type and dwarf spheroidal galaxies, where the dark matter halo core density correlates with the absolute magnitude of a galaxy, i.e., roughly stellar mass content (Kormendy & Freeman 2016, see also Figure 7). Here stellar mass content is traced by BSSs. The dark matter density has been estimated using dynamical mass-to-light ratios M/L_V reported in Muñoz et al. (2018), from which $M_{\mathrm{DM}} = (M_{\mathrm{dyn}} - M_\star) = (M/L_V - M_\star/L_V)L_V/2$, where the factor of 2 follows from the choice of working at half-light radius (i.e., in the following M_{DM}, M_{dyn}, and $M_\star$ are all computed within half-light radius). The contraction of the dark matter halo due to the addition of stars can be corrected by adiabatically expanding the half-light radius. Assuming circular orbits and angular momentum conservation, this gives

$$R'_{h,s} = \frac{M_\star + M_{\mathrm{DM}}}{M_{\mathrm{DM}}} R_{h,s} \qquad (9)$$

(e.g., Blumenthal et al. 1986; Forbes et al. 2018), which has virtually no effect since for this sample of dwarf galaxies $M_\star$ is orders of magnitude smaller than M_{DM}. The approach used here averages the dark matter density over a half-light radius, which is appropriate if (dwarf) galaxies—as it seems—have cored profiles (e.g., Serra et al. 2010; Read et al. 2016; Li et al. 2020). The derived M_{DM} does not account for the effect of tidal stripping of the halos of dwarf galaxies. Nevertheless, this simple methodology returns dark matter densities that typically agree to within a few tens of percent with the values derived from the detailed modeling of Read et al. (2019) for the same galaxies in their sample.

To account for uncertainties, I have repeated the above procedure to derive stellar and dark matter densities using half-light radii and stellar and dynamical masses from McConnachie (2012). Differences with respect to the values obtained using mass-to-light ratios from Muñoz et al. (2018) are typically of a

---

[2] Assuming for simplicity an exponential profile e^{-kx} where k is an integer, there is three-fourths of light within two half-light radii, and two-thirds of this three-fourths is within a half-light.
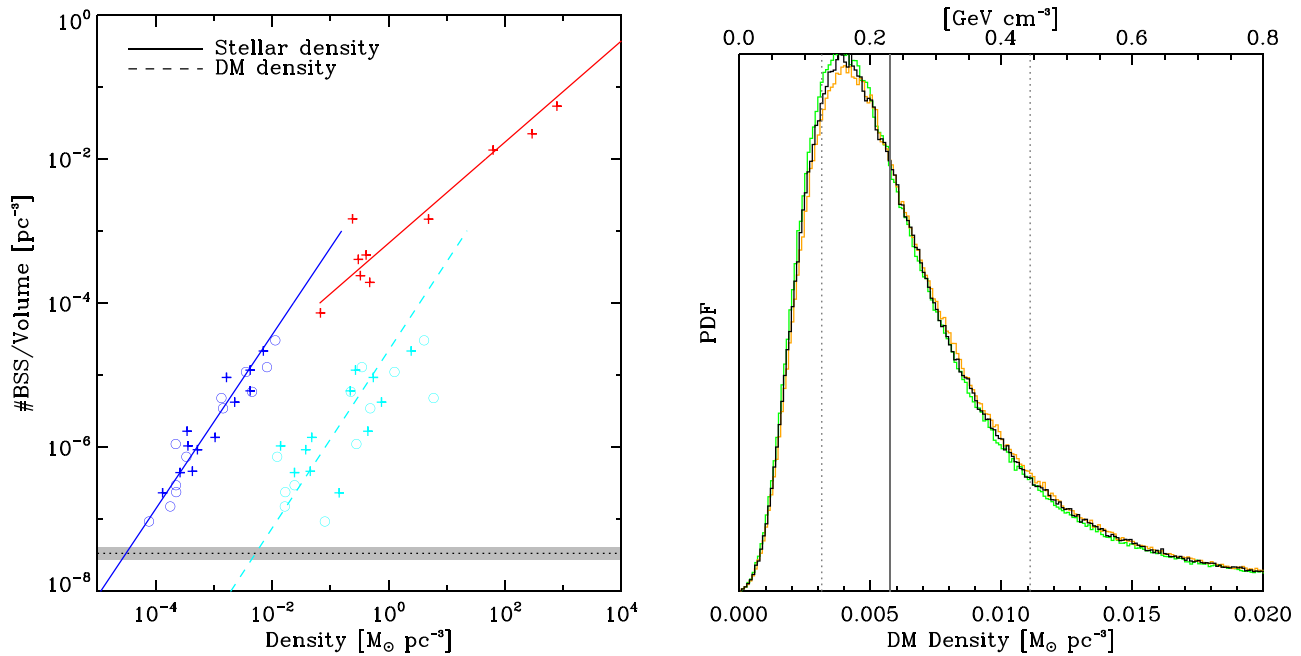
Figure 6. Left panel: volume density of BSSs as a function of stellar density in dwarf galaxies (blue) and globular clusters (red). The volume density of BSSs is found to correlate also with the dark matter density in dwarf galaxies (cyan). Plus signs (open circles) have been derived using data from Muñoz et al. (2018) (McConnachie 2012) as described in the text. All densities are computed within a half-light radius. The dotted line is the volume density of halo BSSs within 2 kpc from the Sun (with 1σ error from the Monte Carlo described in Section 4). Right panel: probability distribution function for the dark matter density within 2 kpc of the solar location. Gray vertical lines are the median (solid) and 16% and 84% values (dotted). Lines of different colors assume different stellar mass-to-light ratios (1, orange; 1.5, black; 2, green).
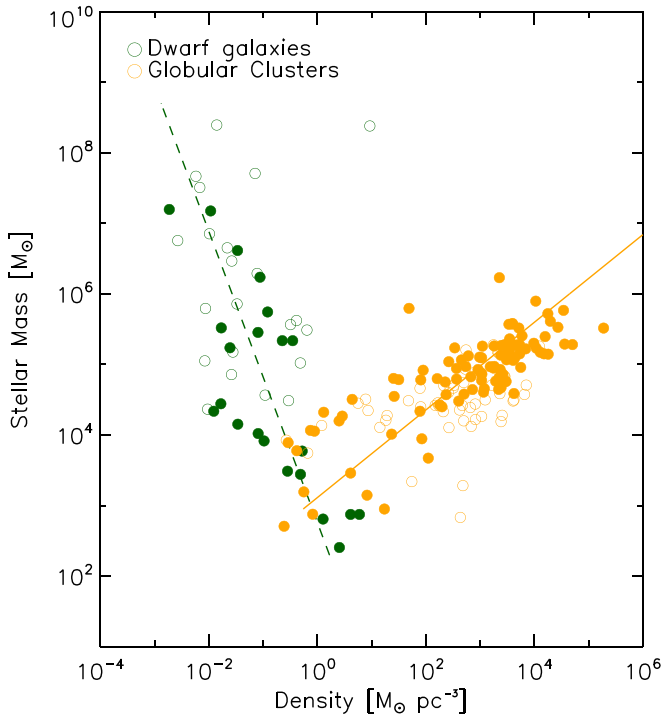
Figure 7. Stellar mass vs. density relation, using the compilation of dwarf galaxies from McConnachie (2012) and globular clusters from Baumgardt & Hilker (2018). For dwarf galaxies, the dark matter density is plotted, computed as described in Section 5. For globular clusters, the stellar density is plotted. Densities and stellar masses are both computed within a half-light radius. Filled circles are dwarf galaxies of the Milky Way (green) and globular clusters (yellow) with masses better than 20%.

few tens of percent. I then generate a million realizations building each time a sample that randomly mixes data from McConnachie (2012) and Muñoz et al. (2018), and I perturb

them by a Gaussian of width equal to half of their differences. The intercept with the local density of halo BSSs (also perturb within its uncertainties) returns a median dark matter density:

$$\rho_{\rm DM} = 0.0058^{+0.0053}_{-0.0026} \, M_\odot \, {\rm pc}^{-3}$$
$$= 0.22^{+0.20}_{-0.10} \, {\rm GeV} \, {\rm cm}^{-3}. \qquad (10)$$

The mean density is instead $0.0076 M_\odot \, {\rm pc}^{-3} = 0.29 \, {\rm GeV} \, {\rm cm}^{-3}$. In can also be appreciated from Figure 6 that varying the stellar mass-to-light ratio by $\pm 0.5 M_\odot/L_{\odot,V}$ has a negligible impact on the inferred dark matter density.

The median (mean) value of $\rho_{\rm DM}$ determined here is in overall good agreement with those recently reported in the literature, which are in the range 0.005–$0.013 \, M_\odot \, {\rm pc}^{-3}$ ($\simeq 0.2$–$0.5 \, {\rm GeV} \, {\rm cm}^{-3}$; see, e.g., Bovy & Tremaine 2012; Smith et al. 2012; Bovy & Rix 2013; Zhang et al. 2013; McKee et al. 2015; McMillan 2017; Sivertsson et al. 2018; de Salas et al. 2019). These methods are based on dynamically modeling the rotation curve or the vertical motion of stars, and in either case a number of assumptions are needed. One of the most important ones is the contribution of baryonic matter to the local dynamical mass, which is nontrivial to determine and strongly correlates with the inferred dark matter density (e.g., Flynn et al. 2006; Sivertsson et al. 2018).

The use of BSSs proposed here is largely independent of the baryonic content (Figure 6, right panel), and the mass estimators used to infer dynamical masses within the half-light radius of dwarf galaxies are believed to be accurate (Campbell et al. 2017; González-Samaniego et al. 2017). The choice of applying a scaling relation inferred from dwarf galaxies to estimate the local dark matter halo is motivated by the similar BSS-to-RGB ratio measured in the local halo compared to dwarf galaxies. Admittedly, however, in dwarf galaxies these scaling relations

are estimated at half-light radii, whereas here they are applied to field stars as a whole.

6. Discussion and Conclusions

The correlation between stellar mass density and volume density of BSSs shown in Figure 6 can be readily understood from the findings of Santana et al. (2013) i.e., the number count of BSSs increases with the stellar mass content of dwarf galaxies, whereas it stays constant in globular clusters. With increasing stellar mass, globular clusters are typically more compact. This means that the volume density of BSSs increases with stellar density, moving from the bottom left to the top right of the red line. For dwarf galaxies, the pathway is opposite. With increasing stellar mass content, the number of BSSs in dwarf galaxies increases, and so do half-light radii. This leads to a decrease of both stellar mass density and BSS volume density with increasing galaxy mass, i.e., moving from the top right to the bottom left of the blue curve. Because the stellar mass content of dwarf galaxies correlates positively with their dark matter content, the same trend still holds when dark matter density is used instead of stellar density. Whether the correlation between the density of BSSs and that of dark matter is indicative of a connection between baryons and dynamics is something worth contemplating (e.g., Sancisi 2004; McGaugh et al. 2016), but beyond the scope of this paper.

The constant number of BSSs as a function of cluster mass ($M_\star$) translates into a decreasing number of BSSs per unit mass ($\propto 1/M_\star$), whereas the number of BSSs per unit mass stays roughly constant in dwarf galaxies ($\propto M_\star^\alpha \times 1/M_\star \sim$ const), where $\alpha \sim 1$ (see Figure 5). The number of BSSs per unit mass can be interpreted as a measure of either formation or disruption efficiency of BSSs. For example, if BSSs are the product of close binaries, it could be argued that in denser stellar systems close binaries are less likely to form, or that closer binaries are more easily disrupted. While addressing these questions is beyond the scope of this paper (see e.g., Momany 2015 for a review), I note that the trends discussed here using BSSs can be traced in the stellar mass versus density relation (Figure 7). This relation is equivalent to the more popular absolute magnitude versus half-light radius relation and shows how the stellar mass of a system has a positive correlation with stellar density in globular clusters and a negative correlation with dark matter density in dwarf galaxies. BSSs are thus tracing these scaling relations, and here I have applied them to the Milky Way halo.

Further investigations are needed to confirm the use of BSSs as a proxy of baryon and dark matter density in the halo, as this technique could be very powerful, e.g., at measuring these quantities across the Milky Way halo on the same scale as in external galaxies. Remarkably, applying to the local Milky Way halo scaling relations inferred for BSSs in dwarf galaxies is able to return both a stellar density and dark matter density that are in overall good agreement with other determinations in the literature. As discussed in the paper, BSSs thus seem to trace stellar mass in low-density, low-metallicity environments regardless if in dwarf galaxies or in the halo. When it comes to dark matter, the correlation between the dark matter core density and stellar mass seen in dwarf galaxies returns a meaningful result also for the local halo. It thus seems that the nearby halo of a bright spiral like the Milky Way can lie on some of the scaling laws for dwarf galaxies. Whether this holds universally or because the nearby halo is largely formed by disrupted dwarf galaxies remains to be seen.

ORCID iDs

Luca Casagrande ● https://orcid.org/0000-0003-2688-7511

References

An, D., Beers, T. C., Johnson, J. A., et al. 2013, ApJ, 763, 65
Arenou, F., Luri, X., Babusiaux, C., et al. 2018, A&A, 616, A17
Baumgardt, H., & Hilker, M. 2018, MNRAS, 478, 1520
Bennett, M., & Bovy, J. 2019, MNRAS, 482, 1417
Blumenthal, G. R., Faber, S. M., Flores, R., & Primack, J. R. 1986, ApJ, 301, 27
Bovy, J., & Rix, H.-W. 2013, ApJ, 779, 115
Bovy, J., & Tremaine, S. 2012, ApJ, 756, 89
Campbell, D. J. R., Frenk, C. S., Jenkins, A., et al. 2017, MNRAS, 469, 2335
Casagrande, L., & VandenBerg, D. A. 2018, MNRAS, 479, L102
Casagrande, L., Wolf, C., Mackey, A. D., et al. 2019, MNRAS, 482, 2770
Choi, J., Dotter, A., Conroy, C., et al. 2016, ApJ, 823, 102
de Jong, J. T. A., Yanny, B., Rix, H.-W., et al. 2010, ApJ, 714, 663
de Salas, P. F. 2020, JPhCS, 1468, 012020
de Salas, P. F., Malhan, K., Freese, K., Hattori, K., & Valluri, M. 2019, JCAP, 2019, 037
Deason, A. J., Belokurov, V., & Sanders, J. L. 2019, MNRAS, 490, 3426
Di Matteo, P., Haywood, M., Lehnert, M. D., et al. 2019, A&A, 632, A4
El-Badry, K., & Rix, H.-W. 2019, MNRAS, 482, L139
Epstein, C. R., Elsworth, Y. P., Johnson, J. A., et al. 2014, ApJL, 785, L28
Evans, D. W., Riello, M., De Angeli, F., et al. 2018, A&A, 616, A4
Flynn, C., Holmberg, J., Portinari, L., Fuchs, B., & Jahreiß, H. 2006, MNRAS, 372, 1149
Forbes, D. A., Read, J. I., Gieles, M., & Collins, M. L. M. 2018, MNRAS, 481, 5592
Fuchs, B., & Jahreiß, H. 1998, A&A, 329, 81
Gaia Collaboration, Babusiaux, C., van Leeuwen, F., et al. 2018a, A&A, 616, A10
Gaia Collaboration, Brown, A. G. A., Vallenari, A., et al. 2018b, A&A, 616, A1
González-Samaniego, A., Bullock, J. S., Boylan-Kolchin, M., et al. 2017, MNRAS, 472, 4786
Gould, A., Flynn, C., & Bahcall, J. N. 1998, ApJ, 503, 798
Gravity Collaboration, Abuter, R., Amorim, A., et al. 2019, A&A, 625, L10
Haywood, M., Di Matteo, P., Lehnert, M. D., et al. 2018, ApJ, 863, 113
Helmi, A., Babusiaux, C., Koppelman, H. H., et al. 2018, Natur, 563, 85
Kippenhahn, R., Weigert, A., & Weiss, A. 2012, Stellar Structure and Evolution (Berlin: Springer)
Knigge, C., Leigh, N., & Sills, A. 2009, Natur, 457, 288
Koppelman, H. H., Helmi, A., Massari, D., Price-Whelan, A. M., & Starkenburg, T. K. 2019, A&A, 631, L9
Kormendy, J., & Freeman, K. C. 2016, ApJ, 817, 84
Kroupa, P. 2001, MNRAS, 322, 231
Kunder, A., Kordopatis, G., Steinmetz, M., et al. 2017, AJ, 153, 75
Li, P., Lelli, F., McGaugh, S., & Schombert, J. 2020, ApJS, 247, 31

Malmquist, K. G. 1922, MeLuF, 100, 1
McConnachie, A. W. 2012, AJ, 144, 4
McGaugh, S. S., Lelli, F., & Schombert, J. M. 2016, PhRvL, 117, 201101
McKee, C. F., Parravano, A., & Hollenbach, D. J. 2015, ApJ, 814, 13
McMillan, P. J. 2017, MNRAS, 465, 76
Moe, M., Kratter, K. M., & Badenes, C. 2019, ApJ, 875, 61
Momany, Y. 2015, The Blue Straggler Population in Dwarf Galaxies, Ecology of Blue Straggler Stars (Berlin: Springer), 129
Momany, Y., Held, E. V., Saviane, I., et al. 2007, A&A, 468, 973
Morrison, H. L. 1993, AJ, 106, 578
Muñoz, R. R., Côté, P., Santana, F. A., et al. 2018, ApJ, 860, 66
Myeong, G. C., Vasiliev, E., Iorio, G., Evans, N. W., & Belokurov, V. 2019, MNRAS, 488, 1235
Preston, G. W., & Sneden, C. 2000, AJ, 120, 1014
Read, J. I. 2014, JPhG, 41, 063101
Read, J. I., Agertz, O., & Collins, M. L. M. 2016, MNRAS, 459, 2573
Read, J. I., Walker, M. G., & Steger, P. 2019, MNRAS, 484, 1401
Reddy, B. E., & Lambert, D. L. 2008, MNRAS, 391, 95

Ruchti, G. R., Fulbright, J. P., Wyse, R. F. G., et al. 2010, ApJL, 721, L92
Ryan, S. G., & Norris, J. E. 1991, AJ, 101, 1865
Sahlholdt, C. L., Casagrande, L., & Feltzing, S. 2019, ApJL, 881, L10
Salpeter, E. E. 1955, ApJ, 121, 161
Sancisi, R. 2004, in IAU Symp. 220, Dark Matter in Galaxies, ed. S. Ryder et al. (San Francisco, CA: ASP), 233
Sandage, A. R. 1953, AJ, 58, 61
Santana, F. A., Muñoz, R. R., Geha, M., et al. 2013, ApJ, 774, 106
Schlegel, D. J., Finkbeiner, D. P., & Davis, M. 1998, ApJ, 500, 525
Serra, A. L., Angus, G. W., & Diaferio, A. 2010, A&A, 524, A16
Sivertsson, S., Silverwood, H., Read, J. I., Bertone, G., & Steger, P. 2018, MNRAS, 478, 1677
Smith, M. C., Whiteoak, S. H., & Evans, N. W. 2012, ApJ, 746, 181
Snaith, O., Haywood, M., Di Matteo, P., et al. 2015, A&A, 578, A87
VandenBerg, D. A., Bond, H. E., Nelan, E. P., et al. 2014, ApJ, 792, 110
Woo, J., Courteau, S., & Dekel, A. 2008, MNRAS, 390, 1453
Wyse, R. F. G., Moe, M., & Kratter, K. M. 2020, MNRAS, 493, 6109
Zhang, L., Rix, H.-W., van de Ven, G., et al. 2013, ApJ, 772, 108